IEEE Access
Multidisciplinary | Rapid Review | Open Access Journal

SPECIAL SECTION ON MILLIMETER-WAVE AND TERAHERTZ PROPAGATION, CHANNEL MODELING AND APPLICATIONS

Received September 2, 2019, accepted October 3, 2019, date of publication October 16, 2019, date of current version October 29, 2019.

Digital Object Identifier 10.1109/ACCESS.2019.2947704

Measurement-Based Millimeter-Wave Angular and Delay Dispersion Characteristics of Outdoor-to-Indoor Propagation for 5G Millimeter-Wave Systems

JUYUL LEE, (Senior Member, IEEE), KYUNG-WON KIM, MYUNG-DON KIM, JAE-JOON PARK, YOUNG KEUN YOON, AND YOUNG JUN CHONG

Telecommunications and Media Research Laboratory, Electronics and Telecommunications Research Institute (ETRI), Daejeon 34129, South Korea

Corresponding author: Juyul Lee (juyul@etri.re.kr)

This work was supported by Institute for Information & Communications Technology Planning & Evaluation (IITP) grant funded by the Korean government (MSIT) [2017-0-00066, ''Development of time-space based spectrum engineering technologies for the preemptive using of frequency''].

ABSTRACT Most outdoor-to-indoor (O2I) propagation studies in millimeter-wave (mmWave) frequency bands have been focused on power loss characteristics such as building penetration and building entry losses. To provide robust traffic services, knowledge of the multipath propagation characteristics is required in the design and evaluation of mmWave 5G systems. In this paper, we investigate the multipath dispersion characteristics of O2I propagation in the angular and delay domains. This study is based on field measurement data conducted at 32 GHz in two different office building sites: traditional building and thermally-efficient building. To derive reliable statistics, we collected measurement data at as many points as possible throughout the building areas (including various environments such as open-space offices, conference rooms, classical closed-room offices, computer labs, halls, corridors, etc). By analyzing power angular and power delay profiles, we found that there were two dominant signal directions and we considered how this property can be utilized in mmWave beamforming. By comparing the angular and delay spreads, we found that the angular and delay statistics do not show any significant differences between the two building measurements. We believe that the property of dominant beam directions, as well as the dispersion statistics (angular and delay spreads), will be useful in the 5G system design.

INDEX TERMS Channel models, 5G mobile communication, millimeter wave propagation.

I. INTRODUCTION

For successful deployment of 5G mobile networks in millimeter-wave (mmWave) bands, relevant propagation/channel characteristics have been studied in various perspectives, not only for system design and planning, but also for frequency sharing and spectrum allocation. Regarding outdoor-to-indoor (O2I) characteristics, studies have been focused more on propagation loss characteristics, such as penetration losses or *building entry losses* [1]–[6] (and references therein), than on multipath characteristics of mmWave O2I propagation [7]–[9]. Knowledge of multipath characteristics, such as delay and angular spreads, are essential for effective system design. For example, delay spread characteristics are typically used in the determination of the length of the cyclic prefix and angular spreads are relevant to beamforming. To provide helpful information for the 5G mmWave system design, in this paper, we investigate such delay and angular dispersion characteristics of O2I propagation based on extensive measurements at 32 GHz. The frequency band of 31.8–33.4 GHz is one of the 5G candidate bands[1] [10].

Relevant to mmWave spectrum allocation for 5G mobile networks, the ITU-R has conducted a frequency sharing study. In doing so, the ITU-R developed a new recommendation on *building entry loss* by integrating over

The associate editor coordinating the review of this manuscript and approving it for publication was Reiner Thoma.

[1]The ITU-R is going to announce the ''official'' 5G mmWave frequency bands in its World Radio Conference (WRC) 2019.

6,000 O2I measurement data sets [11], [12]. According to the Recommendation [11], buildings are classified into two types, depending on the window materials (and not by actual years of construction): *traditional buildings* and *thermally-efficient buildings*. However, this model deals only with the propagation losses and does not provide any information on multipath characteristics such as angular and delay spreads. At a recent ITU-R meeting [13], it was agreed to develop a new recommendation on the multipath characteristics for the O2I propagation. Other standard models, like COST 231 [14], WINNERs [15], [16], 3GPP [17], and ITU-R (Study Group 5)[2] [18], also include O2I propagation characteristics separately from outdoor-to-outdoor and indoor-to-indoor propagation. Among them, the most widely-used for the 5G system design and evaluation is the 3GPP model. While comparing the mmWave 3GPP model [17] to the below-6 GHz 3GPP model [19], we noticed that the angular spread and the delay spread of the O2I propagation have not updated, although most of the other parameters were updated. This may mislead the mmWave 5G system design and evaluation.

When conducting our O2I measurement campaigns, we considered the following three factors affecting O2I propagation: (1) outdoor propagation (from the TX to the building facade), (2) building penetration and (3) indoor propagation (from the glass windows to the RX). We think that the last twos are important, since the outdoor propagation (the first factor) is usually just a line-of-sight propagation and can be characterized by outdoor-to-outdoor propagation. To consider the second factor (building penetration), we conducted the measurement campaigns in two different buildings (traditional-type building and thermally-efficient building). These were carefully chosen to follow the ITU-R building classification guidelines [11]. We tried to maintain a clear line-of-sight from the building facade to the outside TX by lifting the TX to minimize potential foliage effects. We also moved the location of TX in order to maintain near-perpendicular beam incidences on the building facade. To consider the third factor (indoor propagation), we collected as many measurement points as possible throughout the entire building area. More importantly, to obtain multipath characteristics in the delay and angular domains, we collected the data with a 500-MHz wideband channel sounder (with a delay resolution of 2 ns) that can be programmably rotated in 10° steps (with a 0.5° accuracy).

Recently, Bas *et al.* [7] reported O2I propagation characteristics, including penetration loss, delay and angular spreads, based on 28 GHz measurements. However, in their measurements, foliage and beam incidence angle effects were combined with the O2I propagation. That is, the outdoor part (the first factor) in the O2I propagation were combined with the building penetration (the second factor) and the indoor propagation (the third factor). As mentioned before, our work focuses on building penetration and indoor propagation. Compared with ours, their measurement statistics were derived from a limited number of RX points and considered only for traditional-type buildings. Ko *et al.* [8] reported O2I statistics based on the measurements conducted in a lobby area; also, their statistics were from a limited number of measurement points. Tran *et al.* [9] reported the effect of the indoor distance from the window and the effect of the different floor locations. Diakhate *et al.* [20] reported delay spread characteristics for 3, 10, 17 and 60 GHz. Their delay spreads at 17 GHz and 60 GHz are smaller than ours, which might be due to the fact that their measurements were collected in relatively small closed-room environments. Compared to our prior work [21], this paper focuses on multipath characteristics. The prior work focuses on the building entry loss characteristics, although the two papers analyze the same measurement data. Compared to our preliminary conference publication [22], this paper includes details of the measurement campaigns, building penetration loss measurements and angular dispersion characteristics. We believe that the newly-contributed parts from this paper are substantial.

II. MEASUREMENT OVERVIEW

A. MEASUREMENT EQUIPMENT

In the measurement campaign, we utilized our 32-GHz wideband channel sounder, which was built by sharing baseband parts of the existing 28-GHz and 38-GHz sounders [23]. Figure 1 illustrates the configuration of the 32-GHz sounder, and the details of each module are referred to [23]. Table 1 lists the specifications of the sounder. Regarding delay and angular dispersion measurements, the multipath delay resolution of the sounder is 2 ns. The angular resolution (from the servo unit in the antenna positioner) was improved to 0.5° (it was 1° in [23]) by upgrading the antenna positioner unit.

TABLE 1. 32-GHz sounder specifications.

System parameter	Specification
Center frequency	32.4 GHz
Channel bandwidth	500 MHz
PN code length	4095
Signal processing for CIR	Sliding correlation
Multipath resolution	2 ns
Maximum TX power	22 dBm
TX & RX antenna configuration	1×1 SISO

To capture consistent multipath characteristics from various directions, we conducted the measurement repeatedly with three horn antennas (10°, 30°, and 60° horns) and an omnidirectional antenna. The horn antennas are identified with their half power beamwidth (HPBW). The 10° horn antenna was utilized mainly to capture multipath characteristics.[3] Figure 2 shows the antenna pattern of the 10° horn antenna, as measured in an anechoic chamber.

[2]This is a different group in the ITU-R. Reference [11] was developed by Study Group 3 in the ITU-R.

[3]The other antennas were used to ensure the consistency of multipath characteristics and calibrate the beam synthesis characteristics.

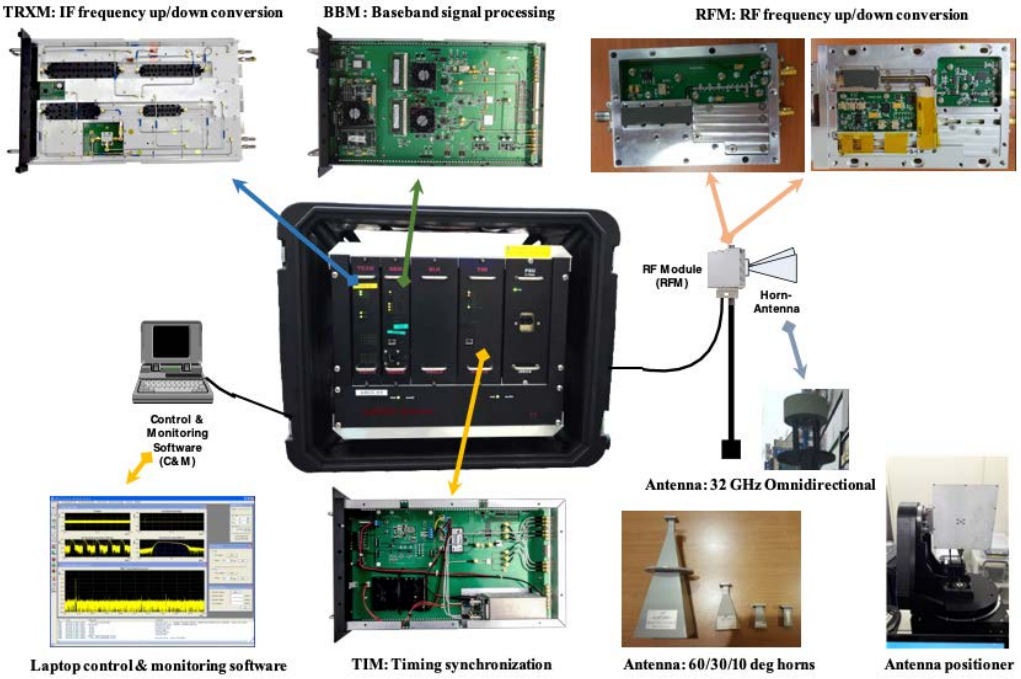

FIGURE 1. ETRI's 32-GHz wideband channel sounder components.

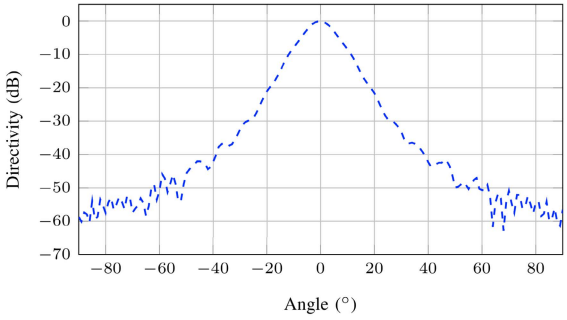

FIGURE 2. Antenna radiation pattern measurements of the 10° horn antenna conducted in an anechoic chamber.

(a) Building A

(b) Building B

FIGURE 3. Buildings for O2I measurements.

B. MEASUREMENT SCENARIOS

For the O2I measurements, we selected two office buildings, as shown in Fig. 3 (identified by Building A and Building B), based on the ITU-R classification [11]. These two buildings were initially built with the same methodology, i.e., all the exterior and the interior structure including inside furnishings, were similar. Recently, Building B was renovated by installing metalized windows. Before conducting the actual O2I measurement, we conducted the glass window penetration loss measurement of the two buildings as described below.

1) GLASS WINDOW PENETRATION LOSS MEASUREMENTS

We employed the measurement setup as seen in Fig. 4, rather than utilizing a controlled chamber (due to the difficulty in acquiring identical glass window material). The TX was located outside the building, whereas the RX was inside the building, as shown in Fig. 5. To avoid multipath reflection effects, we installed narrow-beamwidth horn antennas at both TX and RX. The antennas of TX and RX were aligned to

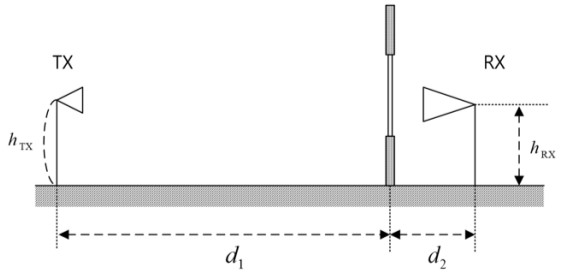

FIGURE 4. Glass window penetration loss measurement setup.

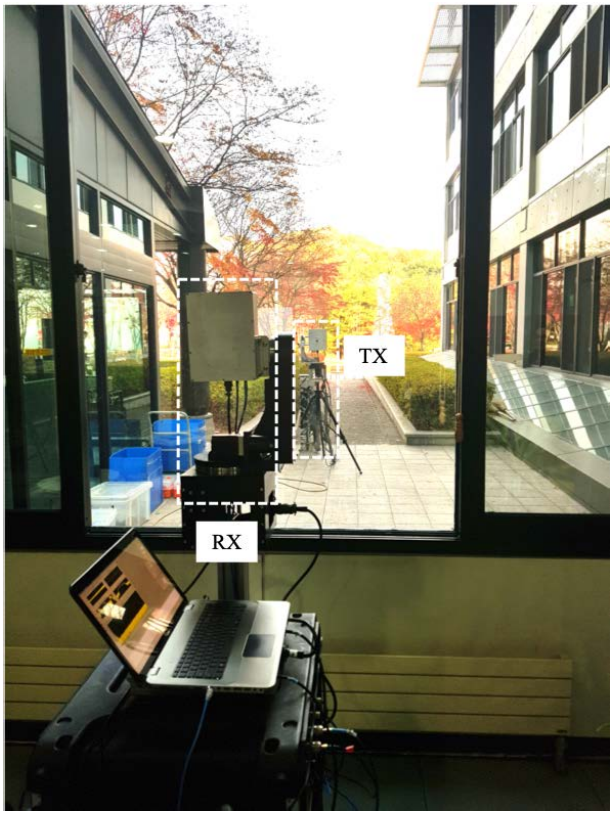

FIGURE 5. Glass window penetration loss measurement.

face each other so that their heights were the same. While the TX was located at numerous d_1 points, the RX antenna was located at three d_2 points: -0.5 m, 0.5 m and 1 m, where -0.5 m refers to the other side (outside the window) as reference measurements.

The penetration loss was calculated by the excess path loss from the free space loss:

$$L_{\text{penetration}} = PL_{\text{measurement}} - L_{\text{free}} \ \text{(dB)}, \tag{1}$$

where $PL_{\text{measurement}}$ is the path loss measurement and L_{free} is the free space loss calculated by

$$L_{\text{free}} = 20\log_{10}\frac{4\times 10^9\pi fd}{c} \ \text{(dB)}, \tag{2}$$

where f is the operating frequency in GHz (i.e., 32.4 in the measurements), d is the TX–RX separation distance in meter and c is the speed of light in m/s. By statistical averaging of all the measured penetration loss, we obtain the penetration loss results shown in Table 2. With the identical measurement setup conducted at the two building sites, the penetration loss difference is 17.4 dB, which is considerable. This is mainly due to the metalized coating in Building B. By comparing multipath characteristics of the two buildings, we will consider the impact of these glass window materials, since the inside of the two buildings are similar to each other.

TABLE 2. Glass window penetration loss measurements.

	Building A	Building B
Glass window penetration loss	10.8 dB	28.2 dB

2) O2I MAIN MEASUREMENTS

As mentioned, the measurements were conducted in Building A and Building B (shown in Fig. 3), with detail information listed in Table 3. These buildings are typical ETRI office buildings, consisting of open-space & closed-room offices, conference rooms, computer labs, halls & corridors, etc.

TABLE 3. Building information.

	Building A	Building B
Planar dimension	72 m × 25 m	58 m × 27 m
No. of floors (above ground)	6	5
Exterior materials	Concrete	Concrete
Window layer	Dual-layer glass	Dual-layer glass
Window coating	None	Metal
ITU-R building type	Traditional	Thermally efficient

In the O2I measurement, to minimize unnecessary effects we considered the followings:

- clear line-of-sight (LOS) between TX and the building facade
- near-perpendicular TX beam incidence
- collection of as many measurement points throughout the whole building area as was feasible

Figure 6 shows the measurement setup. Since there were trees in front of the buildings as shown in Fig. 3, we installed the TX sufficiently high to ensure a clear LOS to the building facade. Furthermore, we selected the floor for RX measurements considering that the height of TX and that of RX can be the same. Detail parameters for the Building A measurements

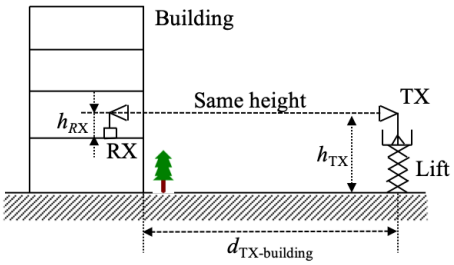

FIGURE 6. O2I measurement setup.

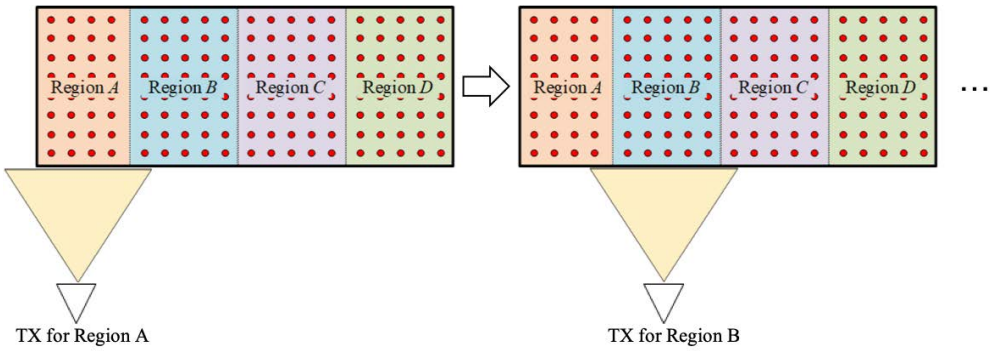

FIGURE 7. Re-location of TX for different RX regions.

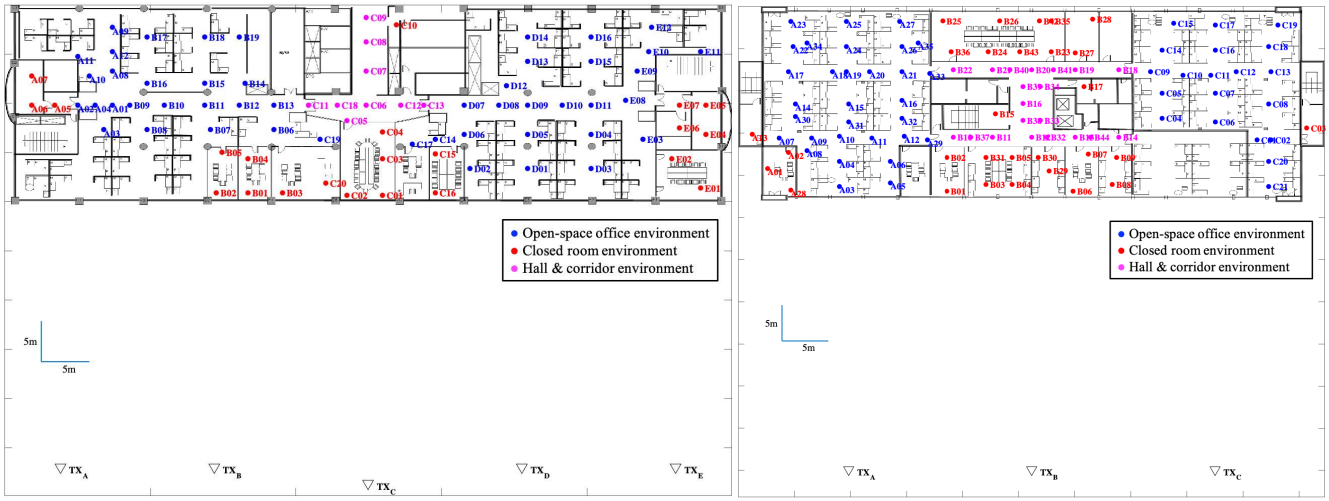

(a) Building A (b) Building B

FIGURE 8. TX positions and RX measurement points (In the office areas, there were numerous office supplies and plant pots that might obstruct the TX signals in some directions.).

were $d_{\text{TX-building}} = 33$ m, $h_{\text{TX}} = 11.7$ m, and $h_{\text{RX}} = 1.5$ m, and those for the Building B measurements were $d_{\text{TX-building}} = 38$ m, $h_{\text{TX}} = 14.7$ m, and $h_{\text{RX}} = 1.5$ m. On the other hand, in the horizontal setup, we relocated the TX as the RX point changes in order to ensure a perpendicular beam incidence. In actual practice, we moved the TX location as the region of RX changed to save measurement time, as illustrated in Fig. 7. The number of RX regions were determined by considering the TX antenna beamwidth, the distance between the TX and the building facade, and the inside indoor structures. We tried to collect as many measurement points as possible throughout the entire building area.[4] Figure 8 shows the actual measurement points along with the building layout and the locations of the TX. As can be seen in the figure, we classified the measurement points into three categories depending on the respective indoor environments: open-space office, closed room, and hall & corridor environments. Measurement data were collected with horn antennas (10°, 30°, and 60° HPBW) and an omnidirectional antenna. All the horn antennas were directionally scanned by rotating the boresight at a 10° step, regardless of the antenna beamwidth. However, due to the numerous outages, we were driven to depend primarily on the 10° horn antenna measurements, with the beamwidth synthesizing technique introduced in [24].

[4]For security reasons, we were not able to access some regions in the two measurement buildings.

III. MEASUREMENT DATA PROCESSING

To process the directionally-scanned wideband measurement data, we need to calculate the power angular-delay profile (PADP), which provides the distribution of power in both angle and delay domain. To do so, if we let $h_\phi(\tau)$ be the channel impulse response (CIR) of the ϕ-direction, we can get the directional power delay profile (PDP):

$$\text{PDP}_\phi(\tau) = |h_\phi(\tau)|^2, \tag{3}$$

where τ is the temporal index in the delay domain. Then, the PADP can be obtained by concatenating directional

data [25]–[27]:

$$\mathrm{PADP}(\tau,\theta)=\sum_{k=1}^{K} I_{\omega}(\theta-k\omega)p_{\theta}(\tau), \tag{4}$$

where ω is the rotation step size, K is the total number of rotation steps, and $I_{\omega}(\theta)=1$ for $-\omega/2\le\theta<\omega/2$ and 0 for elsewhere. The last term $p_{\theta}(\cdot)$ is the θ-directional PDP, which can be obtained by

$$p_{\theta}(\tau)=\mathrm{PDP}_{\phi}(\tau), \tag{5}$$

where ϕ is selected such that $\theta-\omega/2\le\phi<\theta+\omega/2$ and $\phi=k\omega$, $k=1,\ldots,K$. Note that the difference between $\mathrm{PDP}_{\phi}(\cdot)$ and $p_{\theta}(\cdot)$. Depending on the values of K and ω, multiple ϕ's can be found satisfying the conditions. If so, $p_{\theta}(\cdot)$ is suggested to be calculated by averaging multiple $\mathrm{PDP}_{\phi}(\cdot)$. It should be noted that inaccurate PADP will be resulted when the rotation step size ω is larger than the antenna beamwidth. In the measurement setup with the 10° horn antenna, we consider a non-overlapping rotation, i.e., the antenna beamwidth is the same as the rotation step size. We also considered a complete 360° rotation at every measurement point. Figure 9 illustrates an example of PADP from the measurement data collected at "C08" point in Building B, which point can be found in the layout in Fig. 8b.

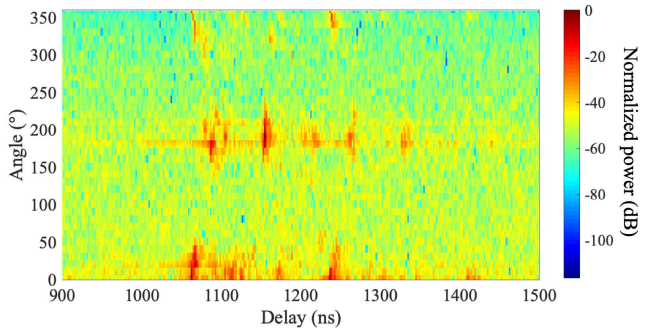

FIGURE 9. An illustration of normalized power angular delay profile (PADP) (from the data at Point "C08" in Building B).

With the PADP, the power angular profile (PAP)[5] and the power delay profile (PDP), which provide the information of power distribution in angle and in delay, respectively, can be calculated by integrating out the other variable:

$$\mathrm{PAP}(\theta)=\int_{\tau}\mathrm{PADP}(\tau,\theta)d\tau, \tag{6}$$

$$\mathrm{PDP}(\tau)=\int_{\theta}\mathrm{PADP}(\tau,\theta)\left(\sum_{k=1}^{K}\delta(\theta-k\omega)\right)d\theta, \tag{7}$$

where $\delta(\cdot)$ denotes the dirac-delta function to account for the discrete nature of rotational sampling. Figure 10 shows examples of normalized PAP and PDP that are calculated from the PADP, shown in Fig. 9.

[5]In some other literature, it is called the power angular spectrum (PAS).

IV. ANGULAR DISPERSION CHARACTERISTICS

One of the important angular dispersion characteristics is the r.m.s. (root-mean-square) angular spread that is the second central moment of the PAP. This provides information about the variability of the mean angle of arrivals. According to [28], the r.m.s. angular spread, which is denoted by AS, is given by:

$$\mathrm{AS}=\sqrt{\frac{\int_{-180^{\circ}}^{180^{\circ}}(\theta-T_A)^2\cdot\mathrm{PAP}(\theta)\left(\sum_{k=1}^{K}\delta(\theta-k\omega)\right)d\theta}{\int_{-180^{\circ}}^{180^{\circ}}\mathrm{PAP}(\theta)\left(\sum_{k=1}^{K}\delta(\theta-k\omega)\right)d\theta}}, \tag{8}$$

where T_A denotes the average angle of arrival and can be calculated by:

$$T_A=\frac{\int_{-180^{\circ}}^{180^{\circ}}\theta\cdot\mathrm{PAP}(\theta)\left(\sum_{k=1}^{K}\delta(\theta-k\omega)\right)d\theta}{\int_{-180^{\circ}}^{180^{\circ}}\mathrm{PAP}(\theta)\left(\sum_{k=1}^{K}\delta(\theta-k\omega)\right)d\theta}. \tag{9}$$

In the calculation of AS, we selected the effective components in PAP that exceed a given threshold, which is set to 20 dB below the peak level, as suggested in [28]. Figure 11 shows the cumulative distribution functions (CDFs) of r.m.s. angular spread (AS) from the two building measurements. We can observe that both Building A (traditional type) and Building B (thermally-efficient type) have almost identical r.m.s. angular spread values, and the measured r.m.s. angular spreads are relatively large. We should be careful in interpreting these results. Relevant to the large angular spread values, we observed that the PAP shown in Fig. 10a has two strong

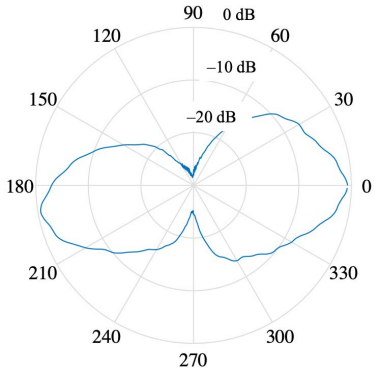

(a) Power angular profile (PAP)

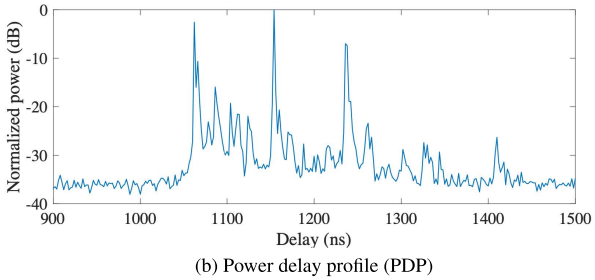

(b) Power delay profile (PDP)

FIGURE 10. An illustration of normalized power angular profile (PAP) and normalized power delay profile (PDP) (from the data at Point "C08" in Building B).

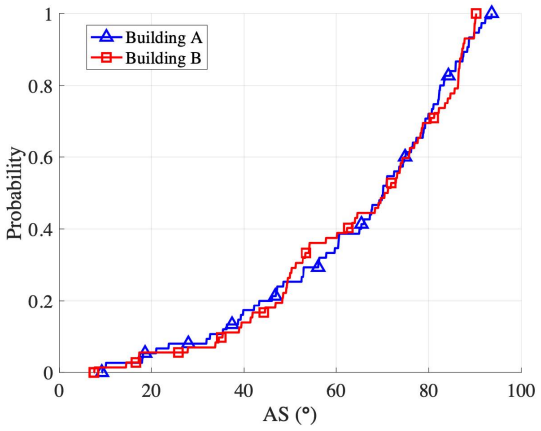

FIGURE 11. Cumulative distributions of r.m.s. angular spread (AS) measurements.

power-arriving directions: one corresponds to the TX beam direction (the 0° direction) and the other corresponds to a reflection from the building structure of the TX beam (in this particular case, near the 180° direction). With this observation, we plotted all the shapes of PAP from all the measurement data,[6] as in Fig. 12. As can be seen, most of the PAPs appears to have two strong power directions in opposite sides.

[6]The points with "×" denote an outage.

This is somewhat clearer with the histograms of such angle difference as shown in Fig. 13. In most cases, the differences are around 180°.[7]

In this respect, we re-calculate the r.m.s. angular spread by limiting its variation range to be less than 180°, which is to capture one strong power directional component. To do so, we replace the range of the integrals in (8) and (9) as:

$$\int_{-180^\circ}^{180^\circ} \quad \text{replaced by} \quad \int_{\hat{\phi}_{\max}-90^\circ}^{\hat{\phi}_{\max}+90^\circ}$$

where

$$\hat{\phi}_{\max} = \arg\max_{\phi} \int_{\phi-90^\circ}^{\phi+90^\circ} \mathrm{PAP}(\theta) \left(\sum \delta(\theta - k\omega) \right) d\theta. \quad (10)$$

This new r.m.s. angular spread is denoted by AS′ and its statistics are shown in Fig. 14. We can observe that the values of AS′ are considerably smaller than those of AS and that Building A has larger AS′ than Building B. We think that this could be due to more signal penetration into Building A contributing to more dispersive multipaths. Due to the shape of PAPs, we should be cautious in interpreting the statistics of AS′ as well (as we did for AS) in that we artificially limit the range of PAP by 180°. In a communication system design

[7]It should be considered that we set up the O2I measurement with near-perpendicular beam incidences.

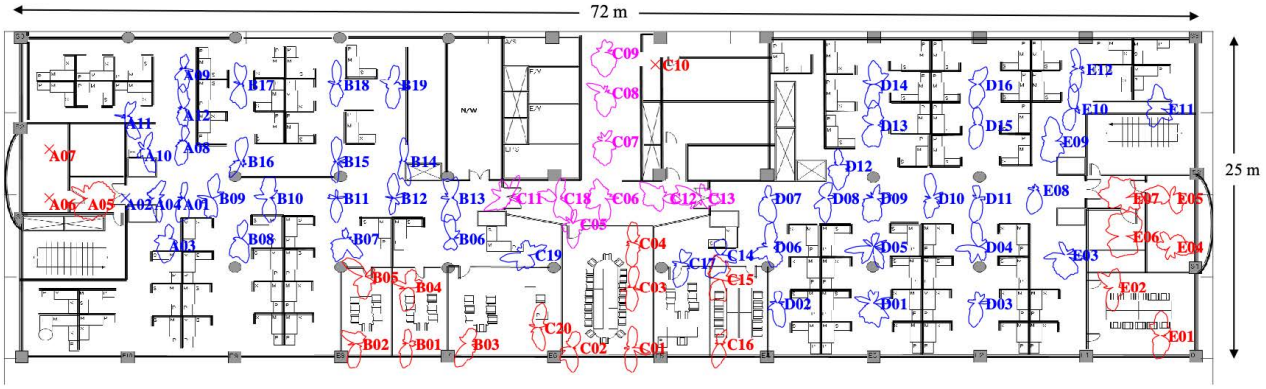

(a) Building A

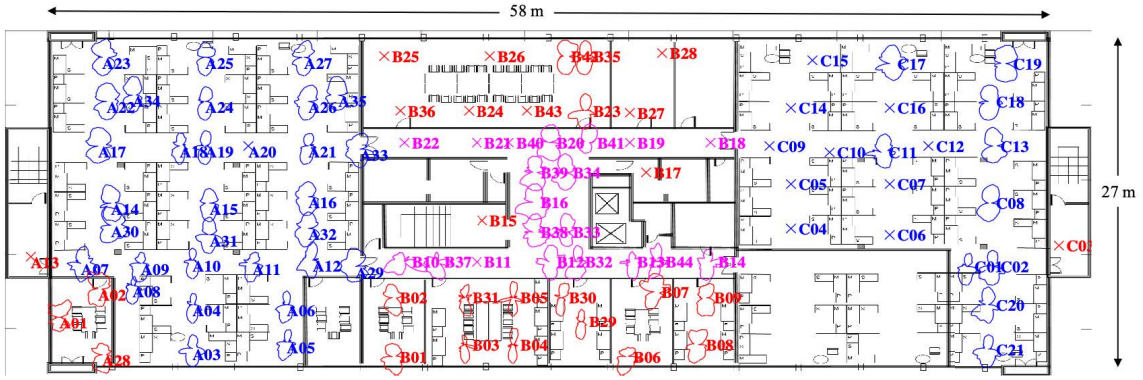

(b) Building B

FIGURE 12. Illustration of power angular profiles with building inside layouts (TX located to the bottom of the facade).

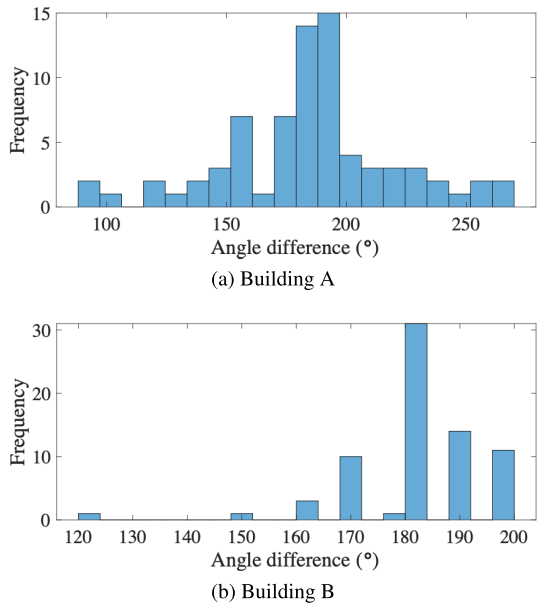

FIGURE 13. Histogram of 1st and 2nd strong power directions.

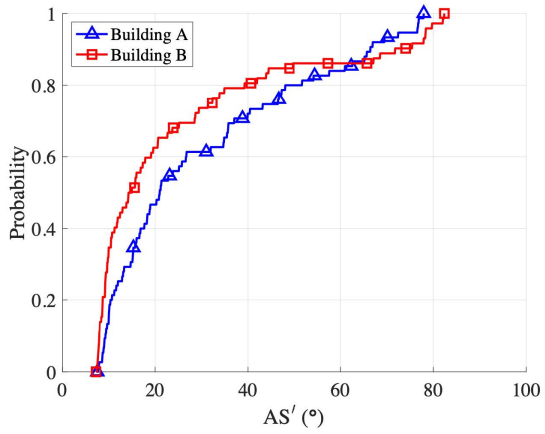

FIGURE 14. Cumulative distributions of AS′ measurements.

TABLE 4. Comparison of median r.m.s. angular spreads.

		Median r.m.s. angular spread (°)
AS	Building A	70
	Building B	71
AS′	Building A	21
	Building B	15
3GPP O2I model [17]		58
Bas *et al.* [7]		43.5
Ko *et al.* [8]		24

perspective, we believe that the statistics of AS′ may be more useful than those of AS. Table 4 shows a comparison of r.m.s. angular spreads with others from the literature relevant to mmWave propagation. First, it should be noted that the 3GPP O2I model data [17] have not updated from [19], which is intended for below-6 GHz frequency bands. Considering the distinctive nature of multipath angular distributions below and above 6 GHz (due to different reflection, penetration, etc) we believe that the 3GPP O2I model should be updated.

Compared to Bas *et al.* [7], which was recently published based on 28 GHz O2I measurements, it should be noted that the measurement environments in [7] are different from ours in that theirs were collected in lobby areas, whereas ours were collected throughout the entire area of office buildings. Objects are generally more closely-spaced in office environments than in lobby areas. This phenomenon also happens if we separate the statistics for individual environment classes, as shown in Fig. 15, in which the indoor propagation environments were identified in Fig. 8. The hall and corridor environments, which are close to the lobby areas, have relatively large values of AS′. Lastly, compared to Ko *et al.* [8], our AS′ of Building A (traditional type) is similar to theirs.

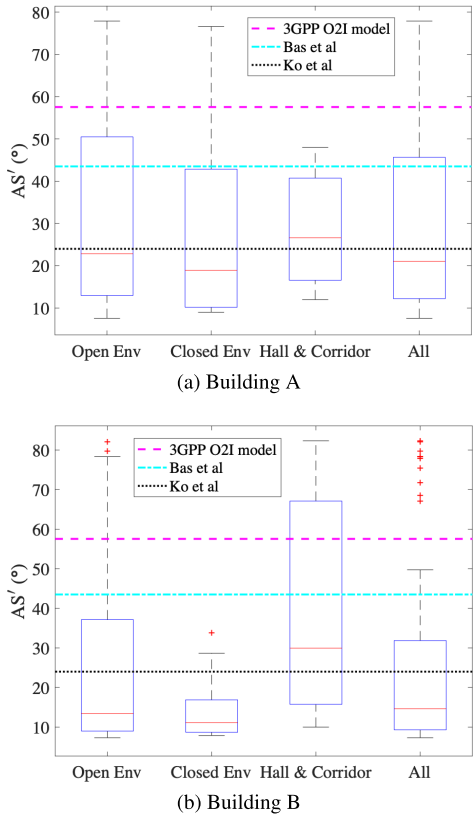

FIGURE 15. Box plot statistics of AS′ compared to the literature (The red line inside the box indicates the median, the bottom and the top denote 1st and 3rd quantiles, i.e., 25th and 75th percentiles, respectively.).

A. CONSIDERATION FOR MMWAVE BEAMFORMING

Thus far, we have investigated fundamental angular spread characteristics from the O2I measurements and observed that there are two strong power-arriving directions in opposite sides. In this subsection, we further investigate how this property can be utilized in mmWave O2I beamforming. In this O2I link environments, where TX is located outside the building and RX is inside the building, the beamforming might be interpreted as the receiver performing the beamforming/combining.

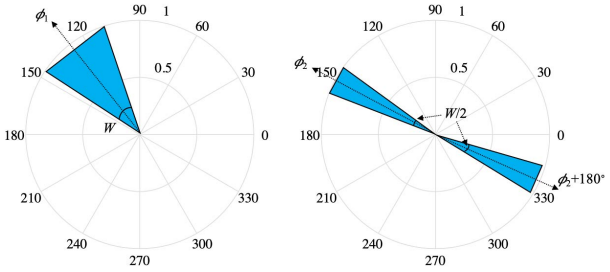

(a) Scheme I: With a single beam direction (b) Scheme II: With two opposite beam directions

FIGURE 16. ***W*-beamwidth beamforming schemes.**

Suppose that we consider two beamforming schemes with W-beamwidth as illustrated in Fig. 16:

Scheme I: one single W-beamwidth beamforming directed to ϕ_1,
Scheme II: two $W/2$-beamwidth beamforming directed to ϕ_2 and $\phi_2 + 180°$.[8]

In both cases, the beam directions ϕ_1 and ϕ_2 are determined to collect the maximum received power in its respective scheme. It should be noted that both schemes have one degree of freedom in the determination of beam direction(s). To evaluate the power ratio that captured with the respective beamforming schemes, we define a ratio as below:

$$R_{\text{angle}}(W) = \frac{P_{\max}(W)}{P_{\text{total}} - P_{\max}(W)} \tag{11}$$

where $P_{\text{total}} = \int_\theta \text{PAP}(\theta) \left(\sum \delta(\theta - k\omega)\right) d\theta$, and $P_{\max}(W)$ for Scheme I and Scheme II can be calculated as follows:

$$P^{(\text{I})}_{\max}(W) = \int_{\hat{\phi}^{(\text{I})}_{\max} - W/2}^{\hat{\phi}^{(\text{I})}_{\max} + W/2} \text{PAP}(\theta) \left(\sum \delta(\theta - k\omega)\right) d\theta, \tag{12}$$

$$P^{(\text{II})}_{\max}(W) = \int_{\hat{\phi}^{(\text{II})}_{\max} - W/4}^{\hat{\phi}^{(\text{II})}_{\max} + W/4} \text{PAP}(\theta) \left(\sum \delta(\theta - k\omega)\right) d\theta + \int_{\hat{\phi}^{(\text{II})}_{\max} + 180° - W/4}^{\hat{\phi}^{(\text{II})}_{\max} + 180° + W/4} \text{PAP}(\theta) \left(\sum \delta(\theta - k\omega)\right) d\theta, \tag{13}$$

where

$$\hat{\phi}^{(\text{I})}_{\max} = \arg\max_{\phi} \int_{\phi - W/2}^{\phi + W/2} \text{PAP}(\theta) \left(\sum \delta(\theta - k\omega)\right) d\theta, \tag{14}$$

$$\hat{\phi}^{(\text{II})}_{\max} = \arg\max_{\phi} \int_{\phi - W/4}^{\phi + W/4} \text{PAP}(\theta) \left(\sum \delta(\theta - k\omega)\right) d\theta + \int_{\phi + 180° - W/4}^{\phi + 180° + W/4} \text{PAP}(\theta) \left(\sum \delta(\theta - k\omega)\right) d\theta. \tag{15}$$

As a result, R_{angle} denotes how much power is captured with the corresponding beamforming, as opposed to the power missed. Figure 17 shows R_{angle} (in a dB scale) depending on the choice of schemes as a function of beamwidth. When the beamwidth is small, Scheme I captures more power than Scheme II. However, we should be aware of the 0-dB line of the ratio, i.e., when the ratio in dB is negative, more power is not being captured with the beamforming. We believe that the operating point should be designed to be at least above the 0-dB line. With Scheme I, we can see that R_{angle} increases but soon gets saturated as the beamwidth increases. However, with Scheme II, the ratio R_{angle} increases as the beamwidth W increases although R_{angle} is small for small W ranges. Besides this advantage of more power reception with the same equivalent beamwidth, Scheme II is more robust in blockage environments. Even if one propagation path is blocked, signals can be still received from the other opposite direction with Scheme II. We believe that this finding of O2I beamforming nature will be helpful in designing and planning of 5G mmWave systems.

[8]The reason for considering this scheme is to exploit the strong power-arriving-direction property while having the same total beamwidth with Scheme I.

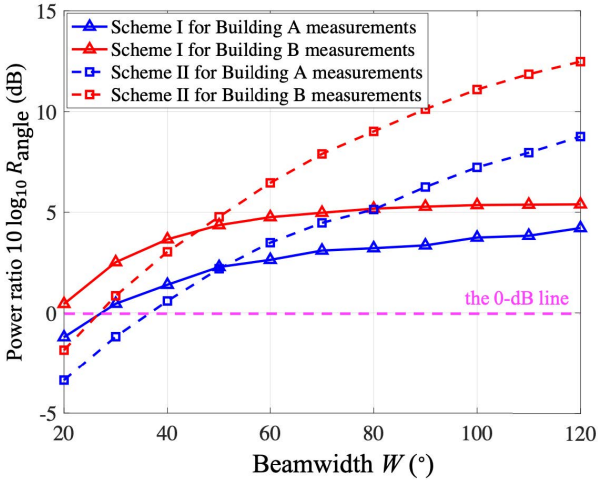

FIGURE 17. **Comparison of beamforming schemes: Ratio of the captured beam power to the non-captured beam power.**

V. DELAY DISPERSION CHARACTERISTICS

As the angular spread represents the variability of angular dispersion characteristics, the delay spread provides a measure of variability in the temporal (delay) domain. This can be calculated by obtaining the second central moment of the PDP [28]. Since we measured directional PDPs, as introduced in (3), we can calculate the W-beamwidth[9] PDP, denoted by $\text{PDP}^W(\tau)$, by using the synthesis algorithm [24]. Then, the W-beamwidth directional r.m.s. delay spread is calculated by

$$\text{DS}^W = \sqrt{\frac{\int (\tau - T_D - \tau_a)^2 \times \text{PDP}^W(\tau) d\tau}{\int \text{PDP}^W(\tau) d\tau}}, \tag{16}$$

where τ_a is the arrival time of the first peak in PDP and T_D is the average delay calculated by

$$T_D = \frac{\int \tau \text{PDP}^W(\tau) d\tau}{\int \text{PDP}^W(\tau) d\tau} - \tau_a. \tag{17}$$

[9]When $W = 360°$, it corresponds to the omnidirectional PDP.

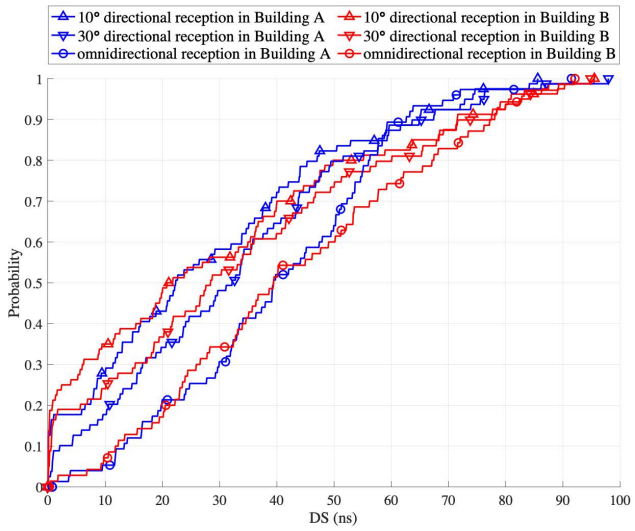

FIGURE 18. Cumulative distributions of the directional r.m.s. delay spread (DS) for different beamwidth receptions.

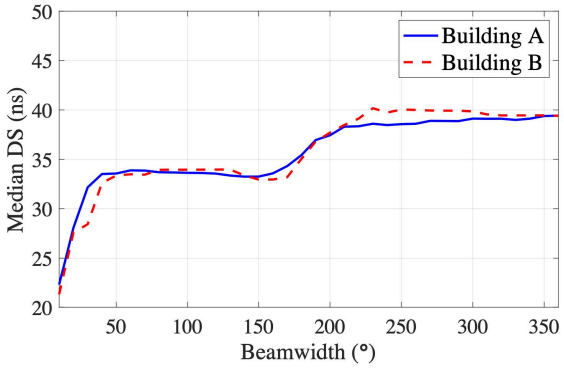

FIGURE 19. Median r.m.s. delay spread with respect to beamwidth.

Figure 18 shows the CDFs of the W-beamwidth directional r.m.s. delay spreads.[10] It is seen that the CDF from Building A measurements and that from Building B measurements are similar. This behavior can be also seen in Fig. 19, which compares the median DS as a function of beamwidth. The reason for the similar DS statistical behavior is, most likely, from a similar interior building and furnishing materials and structures. Among the DS statistics, Table 5 lists a comparison of the median r.m.s. delay spread for omnidirectional reception cases ($W = 360°$) with the 3GPP standard model and reports from the literature. Like the AS statistics in the 3GPP O2I model [17], the DS statistics for mmWave frequency bands have not been changed from the below 6 GHz model [19], which may be unrealistically large. However, the 3GPP model provides the DS statistics for indoor offices (denoted by indoor-to-indoor in Table 5), which is smaller than our DS values. Compared to the literature [7], [8], our DS values are similar or in a similar range.

[10]These results are somewhat different from our prior conference publication [22] in that the DSs of Building B are not larger than those of Building A. This difference was caused by how the outage points were treated in the calculation of the statistics. In this paper, the outages are not included in the statistics, whereas the outages are included in [22] by setting to the maximum values. We now believe that this treatment of discarding outages will be more appropriate in the calculation of DS statistics since the DS value at outage can be assumed to be neither small nor large. However, in the calculation of power statistics, such as penetration loss, building entry loss, propagation loss etc, treating outages by setting to the maximum value will be more appropriate.

TABLE 5. Comparison of median r.m.s. delay spreads for omnidirectional reception.

		Median r.m.s. delay spread (ns)
DS (32 GHz)	Building A	39
	Building B	39
3GPP (32 GHz) [17]	O2I	240
	Indoor-to-indoor	25
Bas *et al.* [7] at 28 GHz		26–48
Ko *et al.* [8] at 28 GHz		36
Diakhate *et al.* [20]	at 17 GHz	16–28
	at 60 GHz	13–14

We further investigated the DS by examining the shape of PDPs. As an example, Fig. 20 shows two PDP samples collected at "C08" and "C18", which are from open-space office environments in Building B. As can be seen, there are regular patterns (apparently from reflections) in both PDPs. We measured the time difference from the first peak of the PDP, as shown in Fig. 20. We tried to determine the source of the regular patterns from the geometry of the measurement layout. As shown in Fig. 21, "C08" and "C18" are marked in the planar layout with the associated dimensions. Assuming that radiowaves propagate at the speed of light (3×10^8 m/s), we calculated the elapsed time returning "C08" from the geometry assuming that radiowave signals are reflecting at both the front-side window (FW) and the back-side window (BW) as follows:

$$\text{Elapsed time (C08} \rightarrow \text{BW} \rightarrow \text{C08)} = \frac{13.4 \times 2}{3 \times 10^8} = 89.3 \text{ ns}$$

$$\text{Elapsed time (C08} \rightarrow \text{BW} \rightarrow \text{FW} \rightarrow \text{C08)} = \frac{13.4 \times 2 + 13.0 \times 2}{3 \times 10^8} = 176 \text{ ns}$$

$$\text{Elapsed time (C08} \rightarrow \text{BW} \rightarrow \text{FW} \rightarrow \text{BW} \rightarrow \text{C08)} = \frac{13.4 \times 2 + 13.0 \times 2 + 13.4 \times 2}{3 \times 10^8} = 265 \text{ ns}$$

We can see that the above three elapsed times are almost identical to the regular timing patterns in Fig. 20a. Likewise, we did the same thing for "C18" as given by:

$$\text{Elapsed time (C18} \rightarrow \text{BW} \rightarrow \text{C18)} = \frac{5.4 \times 2}{3 \times 10^8} = 36 \text{ ns}$$

$$\text{Elapsed time (C18} \rightarrow \text{BW} \rightarrow \text{FW} \rightarrow \text{C18)} = \frac{5.4 \times 2 + 21.0 \times 2}{3 \times 10^8} = 176 \text{ ns}$$

$$\text{Elapsed time (C18} \rightarrow \text{BW} \rightarrow \text{FW} \rightarrow \text{BW} \rightarrow \text{C18)} = \frac{5.4 \times 2 + 21.0 \times 2 + 5.4 \times 2}{3 \times 10^8} = 212 \text{ ns}$$

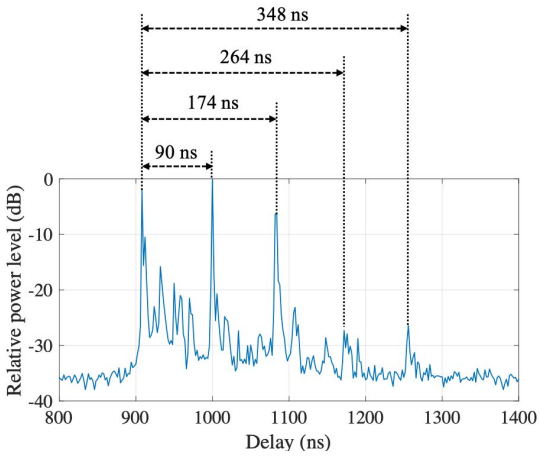

(a) Relative delay information of multipath components at "C08" point

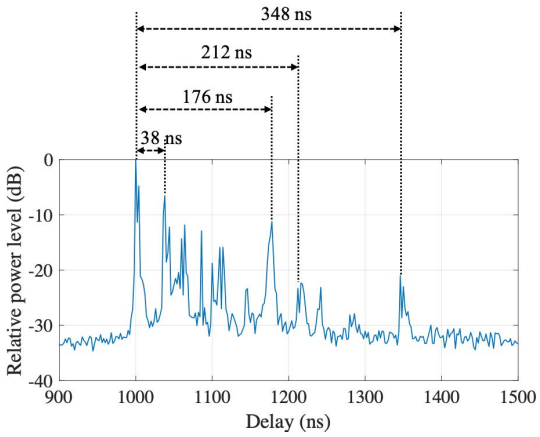

(b) Relative delay information of multipath components at "C18" point

FIGURE 20. PDP at "C08" and "C18" of Building B measurements.

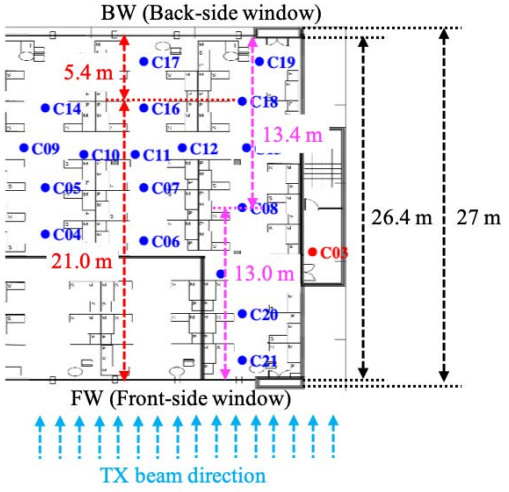

FIGURE 21. Position information of "C08" and "C18" points in Building B.

It is seen that the calculated elapsed time results agree with the relative delay information of multipath components,

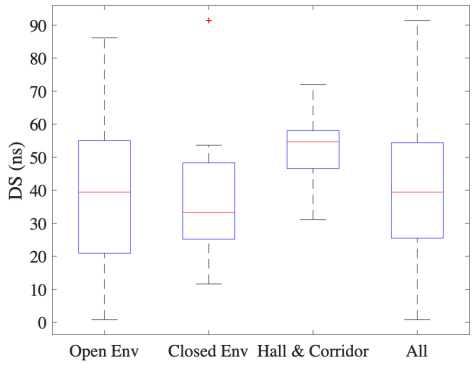

(a) Building A

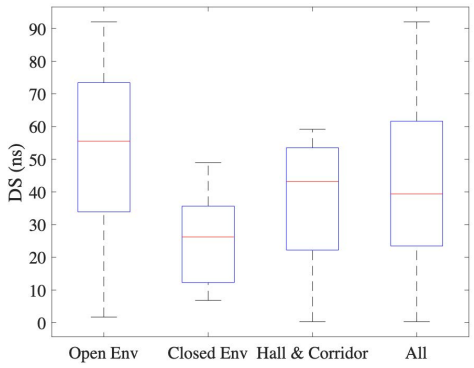

(b) Building B

FIGURE 22. Box plot statistics of DS.

as in Fig. 20b. If high-resolution multipath parameter estimations such as SAGE and RiMAX are applied, a more detailed level of analysis, by decomposing all the individual components of the reflected signal, can be performed. This is left as future work.

Both "C08" and "C18" are points in open-space office environments. It should be noted that the DS statistics will vary, depending on surrounding environments, since the scattering objects will be located differently. Figure 22 shows box plot statistics of DS in terms of indoor environments. Typically, closed-room environments have smaller DS, since objects are typically located close to the receiver, whereas open-space office, hall, and corridor environments have larger DS statistics.

VI. CONCLUSION

By analyzing measurement data, we have investigated the multipath dispersion characteristics of mmWave O2I propagation in two domains: angular and delay domains. In angular domain, we have seen that, in most cases, there are two strong signal directions: one from the TX beam incidence direction and the other from the opposite direction, which appears to be the reflected direction by the back-side window. This has been also clarified in the delay domain by comparing the elapsed delay in measured PDPs to the calculated delay with the building geometry layout. By utilizing this behavior, we considered beamforming schemes for the mmWave 5G

system. Considering that the 3GPP model does not properly provide the delay and the angular spread for O2I scenarios, we believe that the dispersion characteristics will be helpful in the design and evaluation of mmWave 5G systems.

REFERENCES

[1] E. Semaan, F. Harrysson, A. Furuskär, and H. Asplund, "Outdoor-to-indoor coverage in high frequency bands," in *Proc. IEEE Globecom Conf.*, Austin, TX, USA, Dec. 2014, pp. 393–398.

[2] I. Rodriguez, H. C. Nguyen, N. T. K. Jorgensen, T. B. Sorensen, and P. Mogensen, "Radio propagation into modern buildings: Attenuation measurements in the range from 800 MHz to 18 GHz," in *Proc. IEEE 80th Veh. Technol. Conf. (VTC-Fall)*, Sep. 2014, pp. 1–5.

[3] T. Imai, K. Kitao, N. Tran, N. Omaki, Y. Okumura, and K. Nishimori, "Outdoor-to-indoor path loss modeling for 0.8 to 37 GHz band," in *Proc. Eur. Conf. Ant. Prop.*, Davos, Switzerland, Apr. 2016, pp. 1–4.

[4] C. Larsson, F. Harrysson, B.-E. Olsson, and J.-E. Berg, "An outdoor-to-indoor propagation scenario at 28 GHz," in *Proc. 8th Eur. Conf. Antennas Propag. (EuCAP)*, Apr. 2014, pp. 3301–3304.

[5] H. Zhao, R. Mayzus, S. Sun, M. Samimi, J. K. Schulz, Y. Azar, K. Wang, G. N. Wong, F. Gutierrez, Jr., and T. S. Rappaport, "28 GHz millimeter wave cellular communication measurements for reflection and penetration loss in and around buildings in New York City," in *Proc. IEEE Int. Conf. Commun.*, Jun. 2013, pp. 5163–5167.

[6] J. Du, D. Chizhik, R. Feick, G. Castro, M. Rodríguez, and R. A. Valenzuela, "Suburban residential building penetration loss at 28 GHz for fixed wireless access," *IEEE Wireless Commun. Lett.*, vol. 7, no. 6, pp. 890–893, Dec. 2018.

[7] C. U. Bas, R. Wang, S. Sangodoyin, T. Choi, S. Hur, K. Whang, J. Park, C. J. Zhang, and A. F. Molisch, "Outdoor to indoor propagation channel measurements at 28 GHz," *IEEE Trans. Wireless Commun.*, vol. 18, no. 3, pp. 1477–1489, Mar. 2019.

[8] J. Ko, K. Lee, Y.-J. Cho, S. Oh, S. Hur, N.-G. Kang, J. Park, D.-J. Park, and D.-H. Cho, "Feasibility study and spatial–temporal characteristics analysis for 28 GHz outdoor wireless channel modelling," *IET Commun.*, vol. 10, no. 17, pp. 2352–2362, Nov. 2016.

[9] N. Tran, T. Imai, and Y. Okumura, "Outdoor-to-indoor channel characteristics at 20 GHz," in *Proc. ISAP*, Okinawa, Japan, Oct. 2016, pp. 612–613.

[10] *Provisional Final Acts TheWorld Radiocommunication Conference (WRC-15)*, document ITU, Resolution COM 6/20, Nov. 2015.

[11] *Prediction of building entry loss—ITU*, document Rec ITU-R ITU, Jun. 2017.

[12] R. Rudd, J. Medbo, F. Lewicki, F. S. Chaves, and I. Rodriguez, "The development of the new ITU-R model for building entry loss," in *Proc. 12th Eur. Conf. Antennas Propag. (EuCAP)*, London, U.K., Apr. 2018, pp. 1–5.

[13] *Report on the Meeting of Working Party 3K (Geneva, Switzerland, 13–23 May 2019)*, document ITU-R Doc 3K/320-E (2019), Chairman of Working Party 3K, Jun. 2019.

[14] *Digital Mobile Radio Toward Future Generation Systems*, document COST-231, European Cooperation in Science and Technology, Bruxelles, Belgium, 1999.

[15] P. Kyösti, J. Meinilä, L. Hentila, X. Zhao, T. Jämsä, C. Schneider, M. Narandzic, M. Milojevic, A. Hong, J. Ylitalo, V.-M. Holappa, M. Alatossava, R. J. C. Bultitude, Y. De Jong, and T. Rautiainen, *WINNER II Channel Models*, document IST-4-027756 D1.1.2, Version 1.1, Sep. 2007.

[16] P. Kyösti, J. Meinilä, L. Hentila, X. Zhao, T. Jämsä, C. Schneider, M. Narandzic, M. Milojevic, A. Hong, J. Ylitalo, V.-M. Holappa, M. Alatossava, R. J. C. Bultitude, Y. De Jong, and T. Rautiainen, *WINNER+ Final Channel Models*, document CELTIC/CP5-026, 2010.

[17] *Study channel model for frequencies from 0.5 to 100 GHz (Release 15)*, document 3GPP TR 38.901 V15.0.0, Jun. 2018.

[18] *Guidelines for Evaluation of Radio Interface Technologies for IMT-Advanced*, document Rep. ITU-R M.2135-1, Dec. 2009.

[19] *Study 3D Channel Model for LTE (Release 12)*, document 3GPP TR 36.873, Jun. 2015.

[20] C. A. L. Diakhate, J.-M. Conrat, J.-C. Cousin, and A. Sibille, "Millimeter-wave outdoor-to-indoor channel measurements at 3, 10, 17 and 60 GHz," in *Proc. Eur. Conf. Antennas Propag. (EUCAP)*, Paris, France, Mar. 2017, pp. 1798–1802.

[21] J. Lee, K.-W. Kim, M.-D. Kim, J.-J. Park, Y. K. Yoon, and Y. J. Chong, "Millimeter-wave directional-antenna beamwidth effects on the ITU-R building entry loss (BEL) propagation model," *ETRI J.*, Aug. 2019. doi: 10.4218/etrij.2018-0662.

[22] J. Lee, K.-W. Kim, M.-D. Kim, and J.-J. Park, "Directional delay spread characteristics of outdoor-to-indoor propagation based on millimeter-wave measurements," in *Proc. 13th Eur. Conf. Antennas Propag. (EuCAP)*, Krakow, Poland, Apr. 2019, pp. 1–5.

[23] J. Lee, J. Liang, M.-D. Kim, J.-J. Park, B. Park, and H. K. Chung, "Measurement-based propagation channel characteristics for millimeter-wave 5G Giga communication systems," *ETRI J.*, vol. 38, no. 6, pp. 1031–1041, 2016.

[24] J. Lee, M.-D. Kim, J.-J. Park, and Y. J. Chong, "Field-measurement-based received power analysis for directional beamforming millimeter-wave systems: Effects of beamwidth and beam misalignment," *ETRI J.*, vol. 40, no. 1, pp. 26–38, Feb. 2018.

[25] D. Dupleich, F. Fuschini, R. Mueller, E. Vitucci, C. Schneider, V. D. Esposti, and R. Thomä, "Directional characterization of the 60 GHz indoor-office channel," in *Proc. 31th URSI Gen. Assem. Sci. Symp. (URSI GASS)*, Beijing, China, Aug. 2014, pp. 1–4.

[26] D. Dupleich, R. Müller, S. Skoblikov, C. Schneider, J. Luo, G. D. Galdo, and R. Thomä, "Multi-band indoor propagation characterization by measurements from 6 to 60 GHz," in *Proc. 13th Eur. Conf. Antennas Propag. (EuCAP)*, Krakow, Poland, Apr. 2019, pp. 1–5.

[27] X. Yin, L. Ouyang, and H. Wang, "Performance comparison of SAGE and MUSIC for channel estimation in direction-scan measurements," *IEEE Access*, vol. 4, pp. 1163–1174, 2016.

[28] *Multipath Propagation and Parameterization of its Characteristics*, document Rec. ITU-R P.1407-6, ITU, Jun. 2017.

JUYUL LEE (S'07–M'11–SM'19) received the Ph.D. degree in electrical engineering from the University of Minnesota at Twin Cities, USA, in 2010. He was with the Agency for Defense Development, Daejeon, South Korea, from 1998 to 2000. Since 2000, he has been with the Electronics and Telecommunications Research Institute, Daejeon, where he is currently a Principal Researcher with the Telecommunication and Media Research Laboratory. His current research interests include wireless channel modeling, machine learning, and information theory. He has contributed to ITU-R recommendations and reports in Study Group 3 (Propagation) including millimeter-wave propagation models. He is currently the Chairman of the ITU-R Correspondence Group 3K-6, which is responsible for studying the impact of higher frequencies (from 6 GHz to 450 GHz) on propagation models and related characteristics.

KYUNG-WON KIM received the B.S. degree in electrical engineering from Korea University, Seoul, South Korea, in 2009, and the Ph.D. degree in computer and radio communications engineering from Korea University, in 2015. Since 2015, he has been with the Electronics and Telecommunications Research Institute, Daejeon, South Korea, where he is currently a Senior Researcher. His current research interests include channel measurement, radio signal processing techniques, channel parameter estimation, and channel modeling.

MYUNG-DON KIM received the B.S. and M.S. degrees in electronics engineering from Dong-A University, Busan, South Korea, in 1993 and 1995, respectively. Since 1995, he has been with the Electronics and Telecommunications Research Institute (ETRI), where he is currently a Principal Researcher with the Telecommunication and Media Research Laboratory. From 2017 to 2018, he was the Director of the Mobile RF Research Section. He is currently a Project Leader of the Channel Modeling Research Group. His current research interest includes wireless channel measurements and modeling. Since 2006, he has been involved in many projects for development of wideband MIMO channel sounder, field measurements, and channel modeling. He has contributed to the development of ITU-R recommendations and reports in Study Group 3 (Propagation), including millimeter-wave propagation models. Since 2014, he has been the Chairman of the ITU-R WP3K Draft Group 3K-3A, which studies the prediction methods for short-path outdoor propagation in the frequencies from 300 MHz to 100 GHz.

JAE-JOON PARK received the B.S. and M.S. degrees in control and instrumentation from Chungang University, Seoul, South Korea, in 1997 and 1999, respectively. He is currently a Principal Researcher with the Electronics and Telecommunications Research Institute, Daejeon, South Korea. Since 1999, he has been involved in the development of smart antennas for FDD/TDD WCDMA system, the WiBro system for broadband wireless Internet services, and wideband wireless channel model for next generation mobile communication. His current research interest includes channel modeling for millimeter-wave high-speed vehicular wireless communications.

YOUNG KEUN YOON received the B.S. degree in electrical engineering from Chungbuk National University, Cheongju, South Korea, in 1991, and the M.S. and Ph.D. degrees in radio communication engineering from Chungbuk National University, Cheongju, in 1999 and 2007, respectively. Since 2000, he has been with the Electronics and Telecommunications Research Institute, Daejeon, South Korea, where he is currently a Principal Researcher. His current research interest includes radio propagation.

YOUNG JUN CHONG received the B.S. degree from Jeju University, Jeju island, South Korea, in 1992, the M.S. degree in electronics engineering from Sogang University, in 1994, and the Ph.D. degree in electronic engineering from Chungnam National University, Daejeon, South Korea, in 2005. Since 1994, he has been with the Electronics and Telecommunications Research Institute, Daejeon, where he is currently a Principal Researcher. He is currently involved in the research of spectrum engineering. His current research interests include RF circuit, systems and interference analysis. He is a member of KIEES.